SPICAM IR acousto-optic spectrometer experiment on Mars Express

Oleg Korablev,[1] Jean-Loup Bertaux,[2] Anna Fedorova,[1] D. Fonteyn,[3] A. Stepanov,[1,4]
Y. Kalinnikov,[5] A. Kiselev,[1] A. Grigoriev,[1] V. Jegoulev,[1] S. Perrier,[2] E. Dimarellis,[2]
J. P. Dubois,[2] A. Reberac,[2] E. Van Ransbeeck,[3] B. Gondet,[6] F. Montmessin,[2]
and A. Rodin[7,8]

[1] The SPICAM IR spectrometer on Mars Express mission (1.0–1.7 µm, spectral resolution 0.5–1.2 nm) is dedicated primarily to nadir measurements of H_2O abundance. It is one of two channels of SPICAM UV-IR instrument. In this spectrometer we applied for the first time in planetary research the technology of an acousto-optic tunable filter (AOTF) that allowed unprecedented mass reduction for such an instrument: 0.75 kg. SPICAM IR is a point nadir-looking spectrometer with sequential scanning of the spectrum by the AOTF. Sun occultations are performed with a help of dedicated solar port. We describe instrumentation, calibrations, and the modes of operations of the device and discuss its in-flight performances. A brief overview of the scientific measurements includes water vapor measurements and the mapping of intensity of the $O_2(a^1\Delta_g)$ emission at 1.27 µm, described in detail in separate papers. Measurements in reflected solar light allow clear detection of H_2O and CO_2 ices on the surface or in the atmosphere of Mars. We discuss solar occultation measurements by SPICAM and present resulting vertical profiles of aerosol optical depth.

Citation: Korablev, O., et al. (2006), SPICAM IR acousto-optic spectrometer experiment on Mars Express, *J. Geophys. Res.*, *111*, E09S03, doi:10.1029/2006JE002696.

1. Introduction

[2] The SPICAM IR spectrometer covers the spectral range of 1000–1700 nm with spectral resolution of 0.5–1.2 nm, corresponding to a resolving power of 1800–2400. The principal goal of this instrument is to measure water vapor in the Martian atmosphere, spectrally analyzing solar radiation reflected from the surface of Mars and modified by atmospheric absorptions. Water is measured simultaneously with ozone, retrieved from the UV Hartley continuum [*Bertaux et al.*, 2006], for a better description and understanding the chemical coupling H_2O-O_3. The SPICAM instrumentation consists of two blocks: a sensor unit with a total mass ~3.8 kg, which includes the UV and the Near-IR spectrometers, and a data processing unit (DPU, 0.9 kg) providing the interface of these two channels with the spacecraft. The UV imaging spectrometer (118–320 nm, resolution 1 nm, intensified CCD) of SPICAM is primarily dedicated to stellar occultations on Mars. The description of

the UV part of SPICAM, and general issues related to both channel are discussed in paper by *Bertaux et al.* [2006]; in the present paper we concentrate on the IR spectrometer. The IR channel of SPICAM is a separate AOTF spectrometer integrated in the optical block of SPICAM along with the UV spectrometer. As well as the entire SPICAM instrument, the AOTF spectrometer is a product of joint work of three institutions: Space Research Institute (IKI) in Moscow, Service d'Aeronomie du CNRS in France, and Belgian Institute for Space Aeronomy. The spectrometer is developed and built in Russia, it is integrated into SPICAM and calibrated in France; some mechanical parts of SPI-CAM-IR and a solar port are fabricated in Belgium.

[3] In this spectrometer we applied for the first time in planetary research the technology of an acousto-optic tune-able filter (AOTF) that allowed unprecedented mass reduction for such an instrument: 0.7 kg. The electrically commanded acousto-optic filter scans sequentially at a desired sampling, with random access, over the entire spectral range. The absorption bands of H_2O (1.1 µm and 1.37 µm), are registered together with CO_2 bands (1.43, 1.58, and 1.65 µm) allowing a retrieval of relative H_2O contents. The near-IR albedo of Mars in is measured with high spectral resolution revealing characteristic bands of H_2O and CO_2 ices, although it is not possible to distinguish whether these features are of atmospheric (clouds) or surface (ice and frost) origin. As expected, the emission of $O_2(a^1\Delta_g)$ at 1.27 µm, produced in the process of photodissociation of ozone is readily detected by the IR SPICAM, allowing yet another way to measure Mars ozone

[1]Space Research Institute, Moscow, Russia.
[2]Service d'Aéronomie du Centre National de la Recherche Scientifique, Verrières-le-Buisson, France.
[3]Belgian Institute for Space Aeronomy, Brussels, Belgium.
[4]Also at Faculty of Physics, Moscow State University, Moscow, Russia.
[5]Scientific-Production Enterprise AFAR, Zelenograd, Russia.
[6]Institut d'Astrophysique Spatiale, Orsay, France.
[7]Moscow Institute of Physics and Technology, Dolgoprudnyi, Russia.
[8]Also at Space Research Institute, Moscow, Russia.

in addition to UV measurements. The $O_2(a^1\Delta_g)$ emission allows probing attitudes mostly above $15-20$ km; the reaction, producing this emission is strongly depleted by quenching below. The two detectors of the AOTF spectrometer are sensitive to two orthogonal polarizations. We hope to use this capability to study polarization properties of the Martian surface, but the low degree of the surface polarization ($1-2\%$ for typical phase angles) requires very accurate calibration.

[4] On Mars Express mission, the measurements of H_2O in the near-IR 1.37-μm band overlap the spectral coverage of PFS, which measures water vapor in both near-IR (1.37 μm, 1.87 μm, and 2.56 μm) and thermal-IR ($30-50$ μm) ranges [*Formisano et al.*, 2005]. This redundancy is, however, worthwhile because it is important to ensure accurate cross calibration in different wavelength ranges. The 1.37-μm band is the one used by MAWD experiment on Viking orbiters [*Farmer and LaPorte*, 1972], which established the first H_2O season-latitude climatology. With different water vapor measurements on Mars Express it will be possible to compare accurately the Viking climatology based on MAWD data, and the modern climatology based mainly on TES/MGS results in the thermal range [*Smith*, 2004].

[5] A brief description of the IR channel and the expected science return was described by *Bertaux et al.* [2004] and *Korablev et al.* [2002a]; somewhat more detailed description of the hardware is given by *Korablev et al.* [2002b]. Here we present the description of the SPICAM IR spectrometer, its in-flight performances, the various modes of observations, and a brief overview of the measurements on Mars. The measurements of water vapor total contents, data reduction and a seasonal map of atmospheric water vapor are presented in paper by *Fedorova et al.* [2006a]. SPICAM measurements of the $O_2(^1\Delta_g)$ emission at 1.27 μm are discussed in paper by *Fedorova et al.* [2006b]. Solar occultation measurements, detection of the surface frosts, etc., will be a subject of separate studies.

2. Instrument Description

### 2.1. Instrument Heritage and AOTF Usage

[6] The SPICAM instrument on board Mars 96 Russian mission, which did not succeed on escape trajectory to Mars was composed of two packages: one for solar occultation, and another stellar occultation, with the total mass of 46 kg. Within the much more limited payload mass available on Mars Express, the SPICAM team proposed a new instrument, SPICAM Light instrument achieving both the solar and the stellar occultations in the UV with a single compact spectrometer [*Bertaux et al.*, 2000, 2004, 2006]. The proposed IR solar occultation sensor, a grating spectrometer (1.2–4.8 μm, resolution 0.4–1 nm) with a mass of 3.8 kg [*Bertaux et al.*, 2000] was cancelled because of mass constraints of the mission. However, during the early development phase we determined that our mass allocation would permit an extremely lightweight near-IR spectrometer based on AOTF technology. ESA accepted the idea, and this new spectrometer was included as a part of SPICAM. To keep the original solar occultation approach, in the final version of SPICAM both the UV and IR channels acquired the solar occultation sounding capability using a solar entrance port, with the IR channel fed by an optical fiber.

[7] The present version of SPICAM represents the first time an AOTF is used in deep space. AOTF is an electronically tunable optical filter, using the principle of Bragg's diffraction of an entrance beam on the ultrasonic acoustic wave excited within a birefringent crystal. A variable radio frequency (RF) signal, typically below few watts, is applied to a piezoelectric transducer bonded to the crystal. Acousto-optic tunable filters were demonstrated and reported in the literature more than two decades ago and their potential as highly versatile narrow band imaging devices has been recognized for just as long. The operation characteristics of the filters can be found in numerous references [e.g., *Chang*, 1997; *Goutzoulis and Pape*, 1994; *Voloshinov and Gupta*, 1999; *Georgiev et al.*, 2002]. The AOT filters are now technologically mature (the same technology has been extensively developed for beam deflectors and telecommunications), and compact AOTF-based spectrometers and cameras are presently widely used for research and process control. An AOTF camera developed at NASA/GSFC has been used for ground-based observations of planets [e.g., *Glenar et al.*, 1994; *Chanover et al.*, 2003]. There are no moving parts in an AOTF spectrometer, and it can be built as a compact, lightweight, long lifetime, rugged, and reliable device. An AOTF-based spectrometer for aerospace applications (surface analysis) was developed in JPL [*Zhang et al.*, 1995]; the same reference reports positive results of the AOTF radiation hardness testing. Existing references to the use of the AOTF technology in space are consolidated by *Gupta* [1997]. Also, an AOTF spectroimager was flown on Soviet Okean-NHM, and Okean-O satellites in 1986 and 1995. One channel of a submillimeter radiometer on board Swedish satellite Odin launched in 2001 is designated as an acousto-optic spectrometer. However, the principle of this instrument is different from that of the AOTF: a RF-controlled acousto-optic deflector projects light onto a CCD to analyze the RF spectrum [*Olberg et al.*, 2003].

[8] The IR channel of SPICAM Light has passed through the whole chain of space qualification tests, certain requirements for Mars Express being far beyond normal levels, and we are confident that the AOTF technology is mature enough to be widely implemented in future planetary and small-bodies mission.

2.2. Optical Scheme

[9] The AOTF IR spectrometer is included in the UV package, but it is assembled on a dedicated base plate. The optical scheme of the AOTF IR spectrometer is shown in Figure 1. The upwelling radiation from Mars is collected by a telescope, with optical axis parallel to the optical axis of the UV spectrometer and other nadir-looking instruments on Mars Express. The three-lens telescope has a diameter of 30 mm and a focal ratio of 1:1.4. A circular diaphragm of 0.7 mm diameter placed in the focal plane of the telescope forms the field of view (FOV) of 1°. This FOV corresponds to 4.5 km on the surface of Mars when observing from the Mars Express pericenter altitude of about 250 km. The AOTF cell and the associated electronics are placed in a shielded unit. The telescope, the FOV diaphragm and the collimator are assembled in a tube-like structure attached to the AOTF unit. The dimensions of this block, including
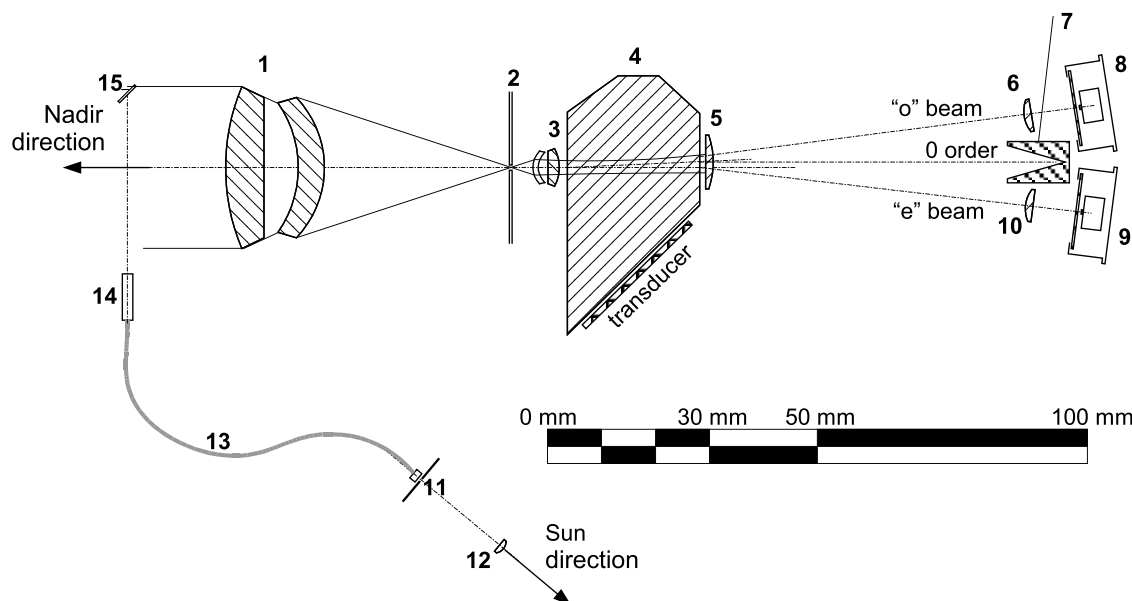
Figure 1. Optical scheme of the IR spectrometer. 1, front-end telescope objective; 2, FOV diaphragm; 3 and 5, collimator; 4, AOTF crystal with actuator; 6 and 10, detector proximity lenses; 7, zero order light trap; 8, detector "1" (ordinary); 9, detector "2" (extraordinary); 11, Sun aperture entry lens; 12, Sun FOV diaphragm; 13, optical fiber; 14, collimating gradient lens; 15, Sun entry folding mirror.

AOTF with its electronics and the telescope are $104 \times 60 \times 40$ mm and its mass is 330 g.

[10] The AOTF is made of tellurium dioxide, TeO_2, or paratellurite single crystal. In the case of SPICAM spectrometer the AOTF is employed in a specific noncollinear configuration [*Epikhin et al.*, 1984], which provides high spectral resolution concomitantly a relatively large acceptance angle. Such a crystallographic configuration, in which both polarizations of the diffracted light are conserved, is unique for TeO_2. The acoustic wave in the crystal is excited by a piezoelectric transducer, with a voltage varying at high frequency (85–140 MHz). The RF drive signal is applied to the transducer placed at the oblique side of the crystal. The length of the active zone (in which the light-sound interaction occurs) is 23 mm.

[11] A collimator forms a quasi-parallel beam in the crystal; the divergence inside the crystal is limited at $\pm 5.5°$. The pupil is minimal in the center of the crystal and does not exceed 3.5 mm at the edges. The incoming light beam is transformed in the birefringent crystal into two partly overlapping output beams. As soon as the acoustic wave is exited in the crystal (RF is turned on) two diffracted beams are observed. The diffracted beams are monochromatic, but tunable with RF, and in orthogonal polarizations. They are deflected to both sides at $7.5°$, the divergence being $5°$. Using an AOTF exit lens ($f = 59$ mm) the output beams are spatially separated from the relatively bright undiffracted orders, which are captured by a central light trap. The angular walkoff (i.e., the drift in the diffracted beam angle as the device is tuned) is insignificant, and there is no need for its compensation in a point spectrometer with relatively large single-pixel detectors.

[12] Two identical detectors with proximity lenses are used to analyze simultaneously the diffracted beams. The detectors are InGaAs photodiodes Ø1 mm (Hamamatsu)

providing with unstabilized cooling (incorporated Peltier elements) with $\Delta T = 25°$. In the present design the noise of the electronic preamplifier is larger than the detector noise at temperature around $0°C$, and we do not use cooling on the Mars orbit.

[13] A dedicated side port lying in the XY plane of the spacecraft and directed at $90°$ from the spacecraft axis $+Z$ (away from the all nadir-looking instruments) is used for solar occultations. The entry optics (a small lens with useful diameter of Ø3 mm and a circular diaphragm) provides an angular FOV of about 4 arc minutes when observing the Sun. An optical fiber delivers the solar light to the IR spectrometer objective. A gradient collimator lens at the output of the fiber and a $45°$ flat mirror mounted at the baffle of the NIR objective completes the design of the solar entry (Figure 1). There is no Sun detector. The pointing to the Sun is provided by Mars Express spacecraft, oriented to the Sun direction with an accuracy of generally much better than 6 arc minutes (spacecraft specification). The side port for Sun observations is normally closed by a shutter, controlled by the DPU, which is opened only during the observation.

[14] Main characteristics of the SPICAM IR spectrometer are summarized in Table 1. The complete IR AOTF spectrometer is shown in Figure 2.

2.3. Electronics

[15] The instrument electronics consists of only a few functional parts: (1) AOTF associated electronics (RF synthesizer and power amplifier) which controls AOTF operation; (2) detector proximity preamplifier board; (3) controller board (including ADC); (4) digital processing Unit (DPU), which provides interface to S/C (common to the whole SPICAM and in a separate block); and (5) power supply (DC/DC). The radio frequency range which deter-

Table 1. Characteristics of the SPICAM IR Spectrometer

Spectral Range	1.0−1.7 μm
Spectral resolution	0.5 nm at 1.1 μm, 0.95 nm at 1.5 μm
FOV	1°
Telescope	Lens type, Ø30 mm
AOTF	TeO_2 aperture 3.6 × 3.6 mm^2, ±3.5°
AOTF RF	85−140 MHz, 0.5−2.5 W
Detector	two InGaAs photodiodes Ø1 mm (Hamamatsu G5832)
Transmission of optics	20%
NER	$\sim 5 \cdot 10^{-5}$ $W/m^2/sr$
Gain control	4 preset gain values
Number of spectral points	2 spectra with different polarizations, 332 to 3984 points each
Dynamic range	2^{16}, rounded to 2^{12}
Power consumption	5 W average
Dimensions	220 × 85 × 65 mm
Mass	≤700 g

mines the wavelength tuning range of the AOTF extends from 80 to 140 MHz. The RF power amplifier includes a circuit controlling the voltage of the output transistor, and therefore the power applied to the AOTF transducer and the AOTF diffraction efficiency when AOTF is on. When AOTF power is off the diffraction efficiency is zero; during this time the AOTF frequency can be changed. RF synthesizer and power amplifier are assembled in the AOTF block that brings all RF into a single shielded volume, minimizing electrical interference.

[16] Each detector photodiode feeds current to a voltage preamplifier having 10 MOhm transimpedance. The output signal is amplified by a variable gain amplifier, relative amplification factors being 1, 3, 8.25 and 26. The measurement scheme does not allow DC offsets at all the individual stages of the amplifier, the bandwidth is limited to 1.6−560 Hz, compromising the signal distortion and the noise reduction.

[17] Output voltages of amplifiers and other analog signals in the system are measured by 12 bit analog-digit converter (ADC) operating in bipolar mode (2048 negative levels and 2048 positive levels). Overall operation, measurement and synchronization of the instrument is provided by a microcontroller (80c32). It receives commands and sends the measured data to the digital processing unit (DPU) of SPICAM. The registration and controlling system is assembled in a single block, with the detector preamplifiers located in the proximity of the detector. The IR channel is powered from secondary voltages provided by SPICAM-UV.

[18] The AOTF serves as an electronically controlled modulator, periodically turning on and off the RF power, and therefore the diffracted light. During a measurement cycle 50% of time RF power on the AOTF is turned on, and the other 50% it is turned off. The chopping period can be set at 1.4, 2.8, 5.6 and 11.2 ms, the same values designating the integration time of the instrument. At each period, 16 measurements (ADC acquisitions) are evenly distributed during the active half-period (AOTF is on and detector is lit) and 16 during the inactive half-period. Each group of 16 measurements is summed together in a 16 bit buffer and the resulting background signal is subtracted from the useful signal. Only the 12 most significant bits out of the resulting value are transmitted to DPU as a spectrum point. A classical synchronous modulation principle is realized, though a conventional electronic lock-in detector chain is

not present. All the data processing, including synchronous detection is performed in digital form. The dead time of the instrument is limited to 120 μs, which is less than 3% of the total integration period.

3. Operations and In-Flight Performances
3.1. Modes of Operation

[19] Mars Express orbit and the observation modes provided by the spacecraft attitude control are described by *Bertaux et al.* [2006]. The IR channel of SPICAM has been operated from January 2004 together with the UV channel. The principal observation configuration for SPICAM IR is nadir orientation; it also operates during slew maneuvers (allowing, in particular, limb observations), solar occultations, and a small number of EPF (Emission Phase Function) observations. Initially SPICAM IR was not operated during stellar occultation, since the faint IR signal from UV stars is far below the detection possibilities of the IR spectrometer. More recently the IR spectrometer has been used with the UV spectrometer during almost all operations of SPICAM in order to better characterize the background signal, and to acquire measurements of the illuminated limb. As of March 2005, the IR spectrometer has performed 826 observations, among them 447 nadir, 94 limb, and 285 solar occultation sequences.

[20] SPICAM IR operates as a point spectrometer and acquires wavelengths sequentially. As a result, each spectrum corresponds to a series of adjacent positions which lie along the orbital ground track. In NADIR configuration the FOV corresponds to ∼5 km from the Mars Express pericenter, and to much larger values, if an observation is performed from higher altitudes away from the pericenter. The ground track speed amounts to 3−4 km/s. It is therefore desirable to keep the time to measure one spectrum as low as possible. A special case is LIMB, or INERTIAL NADIR, when the spacecraft is oriented to the planet near the pericenter, but remains in an inertial attitude. It allows to observe two limbs and a surface track with changing
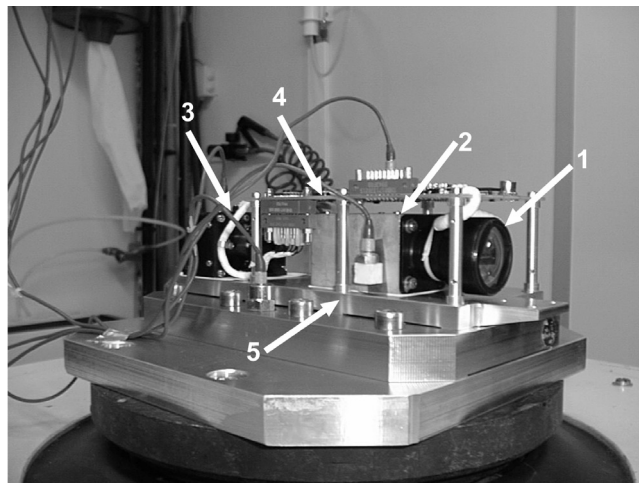
Figure 2. Complete IR channel of SPICAM at the vibration test bench. 1, objective; 2, AOTF unit; 3, detectors unit; 4, electronics; 5, mechanical structure. The overall mass is 750 g.
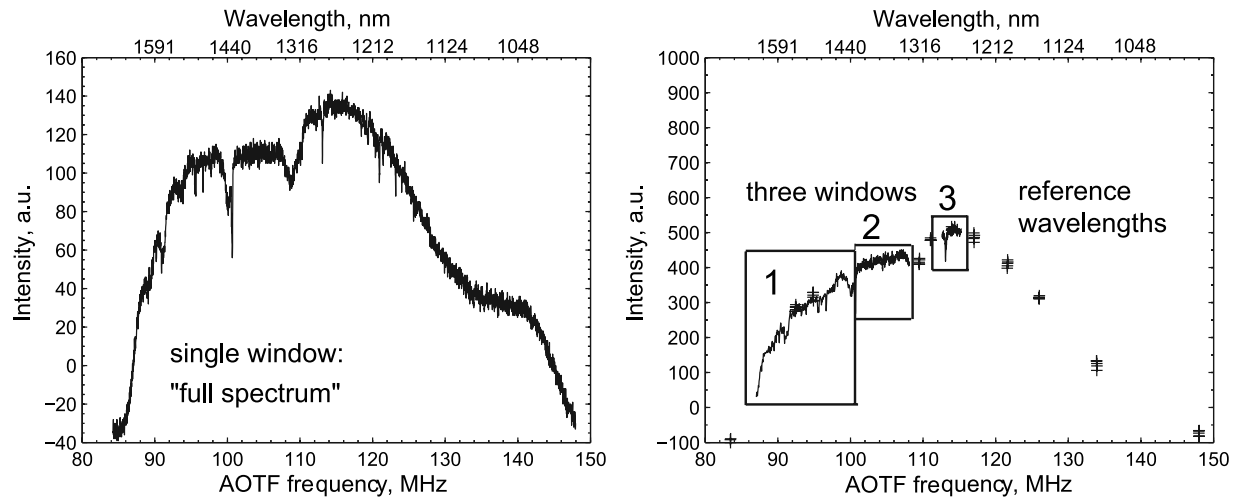
Figure 3. Two spectra of Mars in relative units versus AOTF scanning frequency, illustrating SPICAM IR operation modes. (left) First measurement on orbit 8, a "full spectrum" when the AOTF driving frequency spans the entire range and the AOTF is sequentially tuned to all wavelengths from 1 to 1.7 μm. With a fine sampling such a sequence requires 24 s. (right) Optimized sequence (orbit 1186), in which only the interesting portions of the spectrum are scanned at maximal sampling, less important are scanned with reduced sampling, and the rest of the spectrum is characterized by only a few reference wavelengths; see Table 2.

resolution. The distance to the limb of the planet is much larger, and the FOV typically corresponds to about 30 km. In the INERTIAL NADIR configuration a limb measurement is followed by a disc scan across the planet, allowing sometimes to observe the second limb. In SOLAR OCCULTATION configuration, the distance to the limb may be even larger because the observations are done from distant portions of the orbit. However, the FOV of the solar port is only 4 arc minutes, and the resolution on the limb is typically better than 4–5 km. The vertical speed in limb and occultation observations varies around 2 km/s.

[21] The full scan by the AOTF of the spectral range at fine spectral sampling (3–4 points per element of the spectral resolution) requires 3984 points, and leads to 24-s measurements (the extent of the spectral record on the ground of approximately 5 × 80 km). The monochromatic spot in nadir is nearly circular because the measurement of one spectral point is almost instantaneous (integration time is 5.6 ms). It is possible to reduce the measurement time by sampling only some portions of the full spectrum. The frequency of ultrasonic excitation of the AOTF is controlled by software, and it can be randomly tuned to any wavelength within the spectral range, allowing to optimize the measurement time without compromising the science return. The IR spectrometer can be programmed to scan up to three windows, and to determine for each window the bounds and the spectral sampling. Furthermore, several sets of predefined reference wavelengths are available to characterize the spectral continuum (albedo of the surface, reflectance at limb, extinction, etc.) During the first orbits, we have used the full range of the AOTF, to acquire full spectra at maximal sampling, at the expense of longer sampling intervals. Then, after a first analysis, we restricted the spectra to the most interesting parts, and for this purpose we defined the parameters of the optimized observation modes (see Figure 3). As a result, in most cases we obtain

one spectrum per 4–6 s (the extent of the spectral record on the ground of 5 × 15–20 km), see Table 2.

[22] In the Table 2 we list typical modes of the AOTF employed in the orbit of Mars. Nadir, Limb, etc. designations are arbitrary, and indicate typical occurrences, rather than a firm association with a particular observation configuration of the spacecraft. The difference in source radiation between nadir observations and during solar occultation is largely compensated because of much smaller aperture of the Sun port. We optimized such parameters as gain and AOTF power during commissioning. The integration time of 5.6 ms is chosen as a compromise. At shorter integration time of 2.8 ms the full spectrum at maximal sampling can be acquired faster (12 s), but it results in significantly lower signal-to-noise ratio of the instrument. A longer integration time of 11.2 ms was found impractical and unnecessary, since almost the same improvement in signal-to-noise ratio can be achieved by averaging two spectra. The parameters that we change in flight control mostly the spectral sampling of the AOTF.

[23] For each spectral window, the programmed values are the AOTF excitation frequency, number of points to scan, and the spectral sampling in intervals of 16 kHz. Tuning rates are listed in Table 2 for a typical AOTF temperature of 10°C. The spectral sampling in wavelength changes over the spectral range, but in the first approximation the spectral points are uniformly distributed over the spectral windows. Each measurement progresses from the longest wavelength toward shorter wavelength; the device scans first the window 1, then windows 2 and 3 if they are indicated. Reference wavelengths measurements are then executed in the reverse order, i.e., from shorter to longer wavelength.

[24] The mode Nadir 2, which is mostly used in flight consists of three windows (Figure 3, right). Window 1 (1436–1645 nm) is acquired at somewhat loose sampling and characterizes features of CO_2 and H_2O ices. Windows 2

Table 2. Main Modes of the SPICAM IR AOTF Spectrometer Employed on the Orbit of Mars[a]

		Window 1			Window 2			Window 3			Reference	Duration	Total
Mode	Target	λ_1, nm	λ_2, nm	Points	λ_1, nm	λ_2, nm	Points	λ_1, nm	λ_2, nm	Points	Wavelengths	of sp., s	Points
Nadir 1	full spectrum	997	1697	3984								24	3984
Nadir 2	ice, H_2O, $O_2(a^1\Delta_g)$	1436	1645	277	1339	1440	500	1259	1287	164	set 1, 55 pts	6	996
Limb 1	full spectrum shortened	1049	1645	664								4	664
Limb 2	full + $O_2(a^1\Delta_g)$	1029	1645	500	1259	1287	164					4	664
Limb 3 = Nadir2	ice, H_2O, $O_2(a^1\Delta_g)$ dust	1436	1645	277	1339	1440	500	1259	1287	164	set 1, 55 pts	6	996
Star 1	background	997	1697	332								2	332
Star 2 = Limb 1	background	1049	1645	664								4	664
Sun 1	H_2O	1458	1468	22	1326	1433	536	1286	1307	61	set 2, 45 pts	4	664
Sun 3 = Limb 1	full spectrum shortened	1049	1645	664								4	664
Sun 4 = Nadir 2	ice, H_2O, $O_2(a^1\Delta_g)$, dust	1436	1645	277	1339	1440	500	1259	1287	164	set 1, 55 pts	6	996

[a]Reference wavelengths are stored in the embedded software of the IR spectrometer. In flight we used two sets of reference wavelengths: Set 1 includes wavelengths centered at 997, 1094, 1159, 1198, 1242, 1273, 1305, 1322, 1515, 1553, and 1711 nm with 5 adjacent measurements for each reference wavelength. Set 2 includes reference wavelengths at 997, 1198, 1273, 1515, 1711 nm with 3 adjacent measurements for each and two miniwindows (2×15 points) at 1603.4–1607.5 nm and at 1569–1573 nm.

and 3 are dedicated to H_2O absorption, and $O_2(a^1\Delta_g)$ emission measurements at maximal spectral sampling. A number of reference wavelengths allow to characterize the rest of the continuum. On the limb and in Sun occultations it is desirable to employ the shortest sequences to achieve better vertical resolution. Sparsely filled full spectrum is not of much use since narrow features escape detection. We used such modes only for test purposes, or to characterize the background. A special exploratory mode (Limb 2) was suggested for night side measurements. The most informative and the most employed on the limb is the Nadir 2 mode.

3.2. Dispersion Curve and Spectral Response

[25] Dispersion of the AOTF TeO_2 crystal changes with temperature, and the wavelength assignment of the AOTF spectrometer is expected to change with the drift of the crystal temperature because of internal heat dissipation or because of change in environmental conditions. Two factors contributing to the wavelength drift are the temperature dependence of the sound velocity, and the temperature dependence of the refractive index, the first factor being one order of magnitude stronger. The minimal sound velocity in TeO_2 depends on temperature as $2 \cdot 10^{-4}$ [Ohmachi et al., 1972] but for our specific crystal cut the relative wavelength shift is smaller: $\sim 3 \cdot 10^{-5}$ K^{-1}. The temperature dependence of the AOTF was calibrated on the ground. The unit is equipped with a sensitive temperature sensor in the proximity of the crystal, and the temperature drift can be precisely measured in flight. The wavelength assignment can be therefore accurately corrected according to calibration data.

[26] To determine the wavelength assignment we used a number of laboratory sources of monochromatic light, such as diode and HeNe (1152 nm) lasers, and a low-pressure
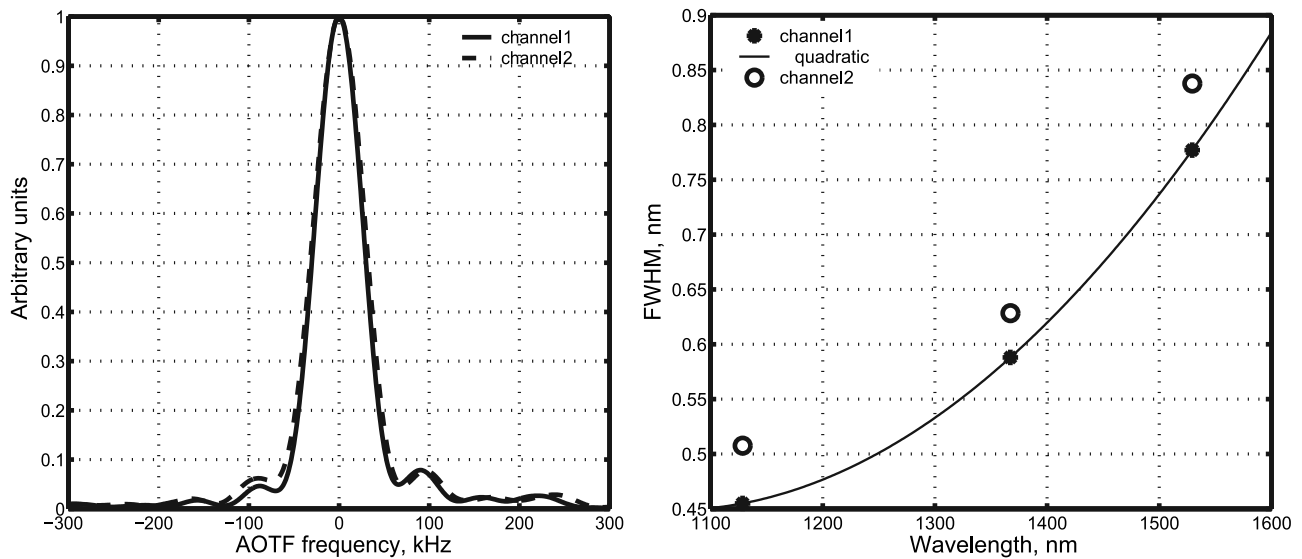
Figure 4. (left) Measured shape of the spectral instrument function as a function of frequency for two channels (theoretically the instrument function of an AOTF is described by $(\sin x/x)^2$ and (right) the FWHM of the central lobe in nanometers in function of wavelength (circles and asterisks indicate measured, and solid curve indicates approximated).

Table 3. Matrix Coefficients for the Wavelengths Calibration Curve (Equation (1))

$n\backslash m$	0	1	2
		Channel 1	
0	74.43	0.0285	10^{-4}
1	$1.367 \cdot 10^8$	0	0
2	$-6.53 \cdot 10^{-11}$	0	0
		Channel 2	
0	71.220396	$4.4824233 \cdot 10^{-3}$	$-5.4920304 \cdot 10^{-6}$
1	$1.3690971 \cdot 10^7$	2464.6217	-3.6228649
2	0	0	0

HgAr pen-ray lamp. The HgAr pen-ray lamp has several strong narrow lines that span representatively the spectral range of our spectrometer at 1128.3, 1356.7, 1367.1, and 1529.3 nanometers. Calibration of the wavelength assignment with the HgAr pen-ray lamp was done in the temperature range of $-20\ldots+40°C$. The dispersion is slightly different for two output polarizations of the AOTF, the wavelength shift being approximately half of a spectral resolution.

[27] The tuning curves of AOTFs have been parameterized by *Chang* [1981], *Gass and Sambles* [1991], *Glenar et al.* [1994], and other authors, but the fitted relationships include multiple parameters some of which are known with a limited accuracy [see, e.g., *Georgiev et al.*, 2002]. We seek for a simple but precise parameterization covering a broad temperature range. We have chosen a quadratic surface representation for frequency and temperature dependence of the AOTF in the form

$$\lambda(f, T) = \sum_{m,n} C_{m,n} T^m / f^n, \quad m, n = 0, 1, 2, \quad (1)$$

and tried to fit the tuning measurement points to this form. Coefficients of matrix $C_{m,n}$ are listed in the Table 3 for the two detectors. The wavelength λ is expressed in nanometers, the frequency f is in kHz, and the temperature measured by the sensor T is in degrees Celsius. The accuracy of this calibration is better than $\pm0.2-0.3$ nm within the range of $1100-1600$ nm. To obtain the above relationship, the ground calibration data were corrected in flight according to positions of solar lines, and controlled against positions of gaseous absorption features. We also take care of a small lag between the sensor count and the true AOTF temperature during transient periods, when the device is warming up. The noise in the first channel (detector 1) is lower, and its dispersion curve is more accurate.

[28] The shape of the instrument's spectral response function was determined with HgAr pen-ray lamp lines, which can be considered as narrow (delta-function). Theoretically, the spectral response function of an AOTF is described as $(\sin x/x)^2$, and the spectral resolution, expressed in the AOTF frequency is approximately a constant within the spectral range. Spectral resolution in wave numbers is modified with the dispersion of the TeO_2. We have accurately measured from several hundred runs the spectral response of the instrument for all the HgAr lamp lines listed above (Figure 4). The spectral response in frequency is very similar for the three strongest HgAr lines at 1129, 1367 and 1530 nm. The full width at half maximum (FWHM) of the central lobe slightly decreases toward longer wavelength, not more than for 10%. The side lobes are also very similar at different wavelengths. The function in Figure 4 is found from averaging of data at 1367 nm. Similar functions were obtained for HgAr lines at 1129 and 1530 nm. The instrument function for intermediate wavelengths is obtained by interpolation. The dependence of the FWHM of the central lobe on the wavelength is presented in Figure 4 (right). The resolving power $\lambda/\Delta\lambda$ of the instrument in the important spectral range of 1.38 μm amounts to 2000, and it is superior to 2400 at 1 μm.

[29] The side lobes of the instrument response function are slightly asymmetric. The function is measured up to the fourth maxima (the central lobe is 0) on the each side, which are both below 0.1% of the maximal transmission. However, the second and the third lobes on the right are about 2.5%. The central lobe contains about 91% of the energy, if we assume the theoretical $(\sin x/x)^2$ approximation beyond the measured range. In this approximation the measured side lobes contain about 6.5% of energy, and the remaining far lobes would contribute as 2.5%. The statistical uncertainty of the measured spectral function is $1-2\ 10^{-3}$, but it is difficult to estimate the impact of the far side lobes from a line spectral source because of a number of potential systematic errors.

3.3. Potential Instrumental Stray Light and Light Leakage

[30] We have noticed that the observed depth of a deep narrow feature of the 1.43-μm CO_2 band in our Mars spectra is systematically lower as compared with synthetic spectra calculated using the measured instrument function (in the interval of ±300 kHz), and Mars general circulation model (MGCM) atmospheric data (see below). The noticeable difference is observed on Mars lowlands, where the estimation of surface pressure gives $0.8-1.0$ mbar lower values than MGCM predictions. There might be different ways to explain this difference, e.g., the scattering by the atmospheric aerosol, but the same effect can be caused by a blur due to far side lobes, or a stray light in the spectrometer. We have chosen a spectrum on the orbit 1023 measured at $L_S = 110.5°$ in aphelion season in Northern Hemisphere (60.5°N, 235°E), where the atmosphere is supposed to be clean from dust or ice clouds [*Smith*, 2004]. We have averaged 10 spectra (local altitude of -3.1 km). To explain the disagreement of synthetic CO_2 band and SPICAM data we have computed four synthetic spectra compared to the same SPICAM spectrum in Figure 5. The synthetic spectrum in Figure 5 (top) is computed with the measured instrument function (±300 kHz), with assumed optical depth of the dust $\tau = 0.5$. The dust is assumed uniformly mixed in the atmosphere. The optical parameters of dust are taken from *Ockert-Bell et al.* [1997]; scattering described by the Heyney-Greenstein phase function with single scattering albedo $\omega_0 = 0.9$ and asymmetry parameter g = 0.63. The spectrum is computed using spherical harmonics discrete ordinate method (SHDOM [*Evans*, 1998]), taking into account the emission, incident and phase angles. The disagreement is apparent as overestimation of the peak absorption by
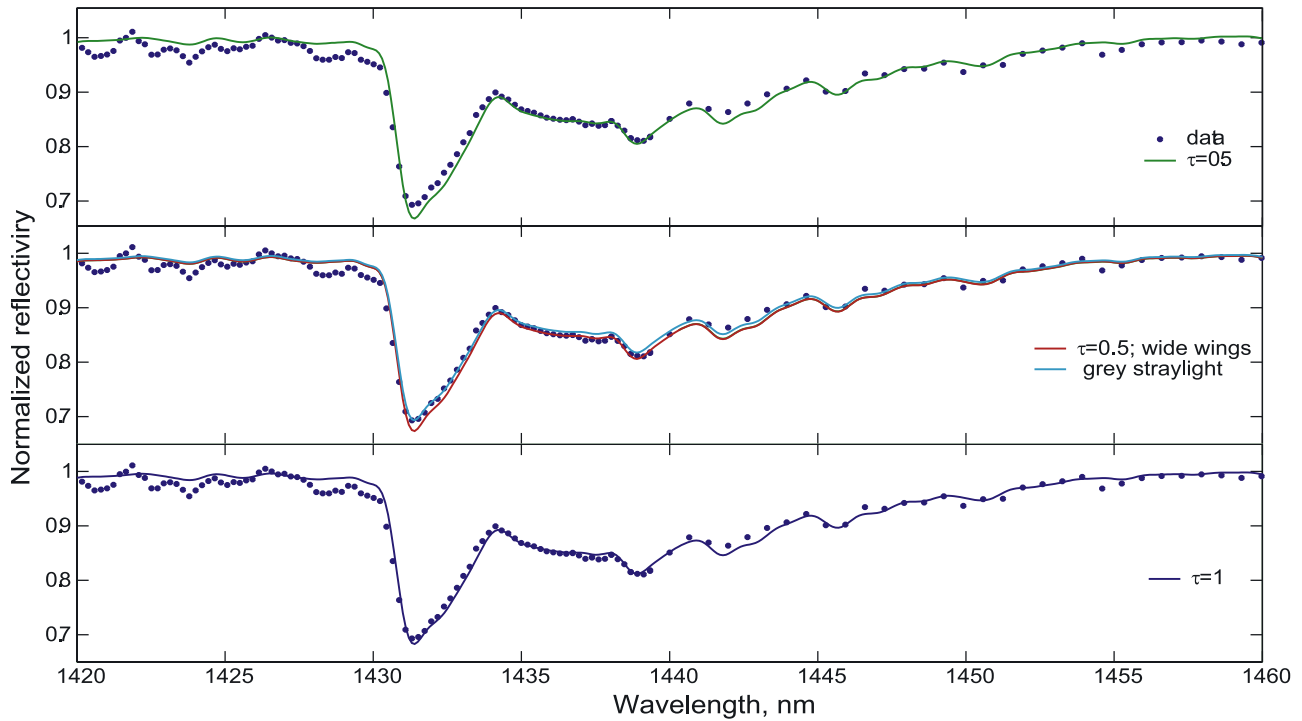
Figure 5. A portion of SPICAM spectrum showing the 1.43-μm band of carbon dioxide compared with four synthetic spectra. The same average SPICAM spectrum is shown in all three plots (blue dot traces). Note the different sampling of SPICAM data (adjacent windows 2 and 1, see Figure 3). (top) Green solid curve indicates a synthetic spectrum computed with the measured instrument function (±300 kHz), with assumed optical depth of the dust of 0.5. (middle) Two synthetic spectra computed for different assumptions. Red solid curve indicates optical depth of the dust of 0.5, and far side lobes of the instrumental function are approximated by a rectangular pedestal of 10^{-3} with a total width of 36 nm, containing 6% of the central lobe. The light blue trace is the spectrum computed with a parasitic "grey" signal of 10% evenly distributed over the spectral range. (bottom) Blue solid curve indicates a synthetic spectrum computed with assumed optical depth of dust $\tau = 1$ and measured instrument function.

CO_2 at 1432 nm in the model spectrum. Poor agreement on the left is most likely due to solar lines (see discussion about the theoretical solar spectrum below). The absorption by H_2O was accurately accounted for in this exercise, but the main H_2O band lays shortward of the wavelength range of Figure 5. Then we introduced some stray light in the model (Figure 5, middle). One spectrum (red trace) is computed for the same amount of dust in the atmosphere, approximating far side lobes of instrumental function by a rectangular pedestal of 10^{-3} extending to ±2000 kHz (total width 36 nm) from the central lobes, and containing 6% of the central lobe of the instrumental function. Another spectrum (light bleu trace) assumes a parasitic "grey" signal of 10% evenly distributed over the spectral range. The assumed wide side lobes agree with the upper limit imposed by our calibrations, but this additive to the instrument function is still insufficient to fit the data. In turn, the stray light of 10% distributed over the spectrum allows to fit the measurements well, even with a small overrun. Finally, a synthetic spectrum shown in Figure 5 (bottom) is computed with assumed optical depth of the dust $\tau = 1$, and the measured instrument function (no far side lobes). This model is in reasonable agreement with measured SPICAM spectrum, but such a high amount of dust in this season is far beyond the limits imposed for

lowlands on Mars by lander measurements [*Colburn et al.*, 1989; *Smith and Lemmon*, 1999].

[31] The physical reason for a continuous stray light in the AOTF spectrometer with synchronous modulation is uncertain. A stray light arising from scattering at optical elements or stops ahead of the diffraction, or at the surface faces of the crystal, or internal to the crystal is subtracted from the diffracted light each time the AOTF is off (see section 2). Another possibility could be a spurious diffraction at the second and even at the third harmonics of the RF. Indeed, at 1.43 μm (RF = 100 MHz) the second harmonic of the RF corresponds to 760-nm range, where the solar flux is 3.5 times more intense (but the spectral sampling may be also smaller). The InGaAs detector is sensitive to the visible light, and there is no IR or red low-pass filter in the instrument. A theoretical estimation of such parasitic diffraction is difficult, since the acoustic and electric impedances outside of the AOTF design tuning range are misaligned. We have tried to detect the spurious visible light in the instrument using a combination of glass filters and a 10-cm slab of distilled water. Such a filter is transparent in the visible, and suppresses completely the near-IR light above 1.15 microns. We have detected no trace of the stray light, exploring the whole dynamic rage of the
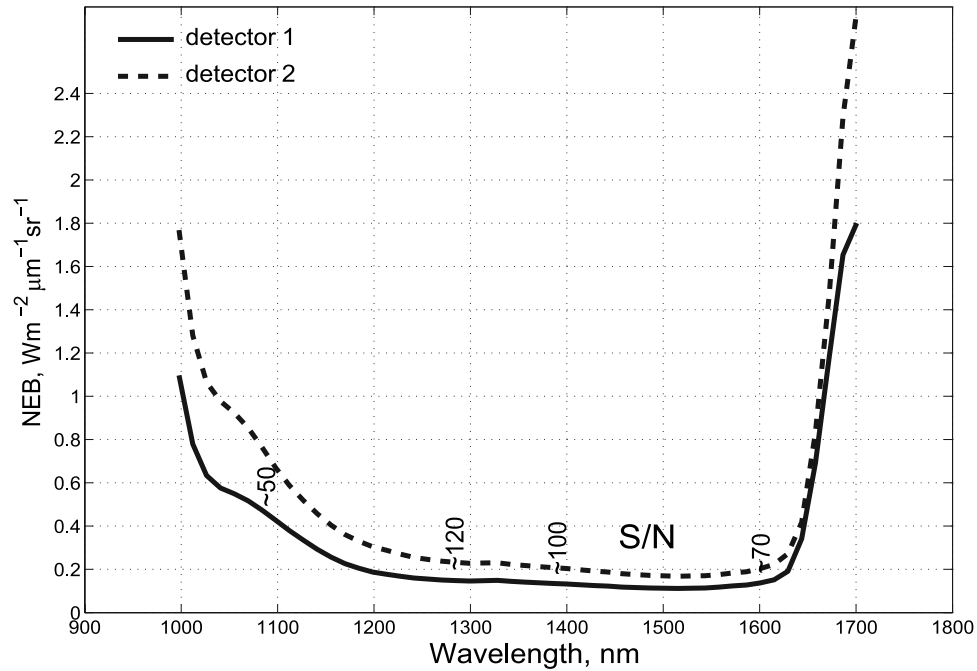
Figure 6. Noise equivalent brightness (NEB) of the SPICAM IR AOTF spectrometer in the spectral range 1–1.7 μm for 5.6-ms sampling time. Approximate signal-to-noise values for the sunlight reflected from the surface of Mars are indicated near the curves.

instrument, with an accuracy superior to 10^{-3}. The same impact as the 10% stray light can be modeled with far side lobes, e.g., with a 60-nm 10^{-3} rectangular pedestal of the instrument function, or with some trapezoidal pedestal. The low-level extended pedestal, or the passband leakage may be caused by imperfect RF coupling into the crystal, or by scattering of the acoustic wave in the crystal (imperfect absorber). We assume that the far side lobes are the most likely reason of the blur suspected in the Mars spectra.

3.4. Absolute Calibration and Signal-to-Noise

[32] During the first year of SPICAM in orbit, the ground calibration data and the flight data were reanalyzed and an updated calibration database of the IR instrument has become available. Because of discrepancies between ground test results and subsequent in-flight tests of SPICAM IR, it was necessary to corroborate the in-flight recalibration by a comparison with OMEGA mapping spectrometer data [*Bibring et al.*, 2004], taking into account the differences in instrument specifications. One OMEGA pixel is only 4.1 arc min against 1° FOV of SPICAM, in turn spectral sampling of OMEGA is 13 nm in the spectral range of interest against 0.6 nm for SPICAM. We compared SPICAM spectra convolved to OMEGA spectral resolution with OMEGA spectra integrated over the SPICAM FOV for a few orbits (30, 68, 278, 103, 368) with relatively homogenous surface albedo. The chosen orbits correspond to different parameters of SPICAM operation. This recalibration procedure resulted in a responsivity scale factor $k(\lambda)$, which relates target radiance (W/m^2/μm/sr) to SPICAM response in ADU. The reported accuracy of OMEGA calibrations is superior to 15%. SPICAM noise-equivalent brightness (NEB) for a sampling of 6 ms is presented in Figure 6 and reaches in the best case the value

of 0.1 W/m^2/μm/sr that is better than the value in Table 1, estimated from laboratory measurements using a calibrated tungsten lamp and sun atmospheric measurements [*Korablev et al.*, 2002b].

3.5. Dark Signal

[33] The in-flight performance of the AOTF spectrometer does not differ substantially from what was expected from its ground testing and calibrations. The noticeable exceptions are a slight modification of the instrument background and the measurements in solar occultation mode.

[34] The measurements of the AOTF spectrometer are based on digital synchronous detection (see section 2), and for each measured point the dark signal is subtracted from the useful signal. Therefore, theoretically, the background signal is zero, unless there is a synchronized optical or electrical interference. While the former is unlikely, the latter comes from the RF driver of the AOTF itself. This kind of interference depends on RF frequency and power, and forms a characteristic pattern as a function of wavelength. This pattern, well characterized on the ground, has changed after the launch with a minimum, which appeared around 1.35 μm. Also, we noticed slight modifications of the background in function of observation mode (Nadir, Limb, etc.), due most likely to the modification of thermal regime. A special effort has been dedicated to characterize the background behavior in flight, in function of particular observation modes, and including the dependence on temperature and other parameters. To support this study, the IR spectrometer is maintained on during most of operations when no significant signal in the IR is expected.

[35] As soon as the background signal is determined, the correction procedure is trivial and consists of subtraction of the averaged smoothened background signal from each
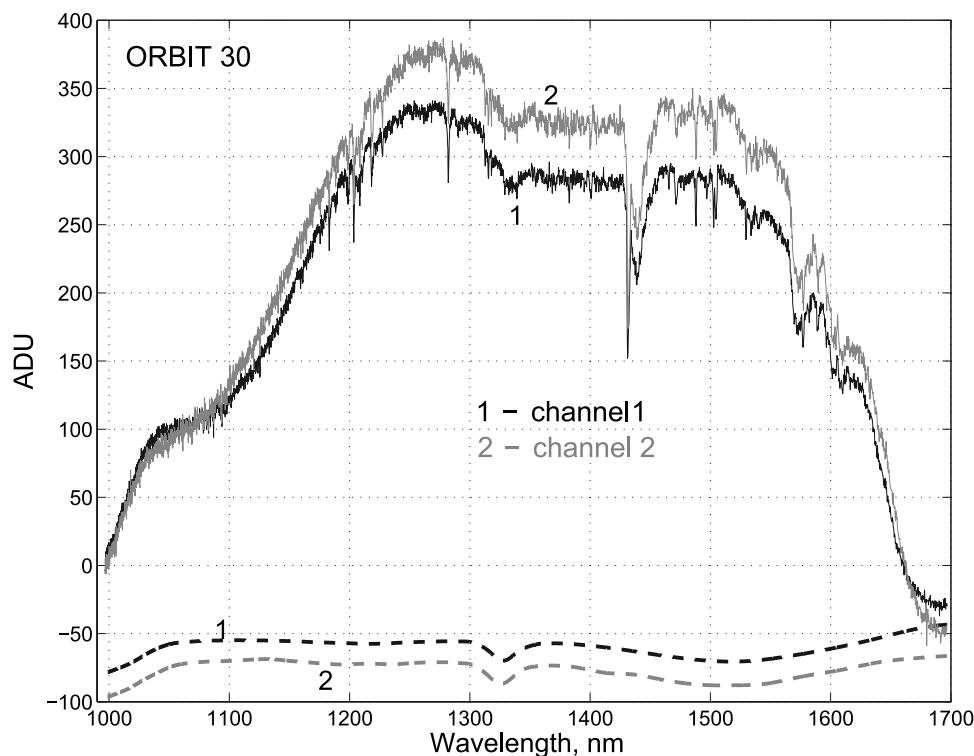
Figure 7. Raw SPICAM IR data measurements in function of wavelength. Two individual spectra for two different polarizations are shown. Dashed curves are negative dark signals for both channels.

measured spectrum (Figure 7). It should be noted that uncertainties in the background signal do not strongly influence the retrieval accuracy for robust quantities, such as water vapor content. An accurate knowledge of the background is most relevant for distinguishing spectra that differ by less than 1–2%, as would be necessary for polarization studies.

4. Measurements

4.1. Nadir Spectrum

[36] A typical calibrated spectrum measured by SPICAM IR in Nadir geometry for an early orbit 30 is presented in Figure 8. The main features of the spectrum are the spectral slope toward the longer wavelengths due to solar spectrum, a large number of Fraunhofer lines, and some atmospheric absorption features, the most prominent being the CO_2 absorption bands at 1.43, 1.58, and 1.6 μm, and the H_2O absorption band around 1.37 μm (Figure 9).

[37] To construct a synthetic model relevant to the observed spectrum we have to account for gaseous atmospheric absorption, surface albedo, aerosol extinction, and the solar spectrum. Gaseous absorption is computed line-by-line using the spectroscopic database HITRAN-2000 [*Rothman et al.*, 2003]. Temperature and pressure profiles are taken from the European Martian Climate Database (EMCD) MGCM [*Forget et al.*, 1999]. We used the same model for the surface pressure (available on the grid of 1/16°), and calculate the air mass for each measurement. The vertical distribution of water in the atmosphere is assumed uniformly mixed up to the saturation level (defined by model temperature profile) and limited by the saturation above.

[38] An important issue is an accurate solar spectrum, because numerous solar lines mix up with the signatures of atmospheric gases. There are few sources of high-resolution solar spectrum in spectral range of interest. A theoretical spectrum by *Kurucz* [1995] and a measured SOLSPEC spectrum [*Thuillier et al.*, 2003] are at the limit of the required spectral resolution. A special effort to construct a high-resolution solar spectrum was done by the PFS team [*Fiorenza and Formisano*, 2005]. We now use the latter spectrum for the retrievals, but we still found several disagreements among this spectrum and solar features in SPICAM spectra.

[39] The distinct water vapor absorption band near 1.37 μm (Figure 9) allows to measure water vapor contents in the atmosphere of Mars. It is well resolved, and the retrieval is possible even if the shape of the spectrum in this range is significantly modified with uneven spectral continuum. Presently we do not take into account the atmospheric aerosol for routine analysis of the nadir spectra. We compare calibrated SPICAM spectra to a model including solar spectrum and synthetic gaseous absorption, and retrieve a continuum spectrum approximated by a smooth function. This continuum is a combination of the surface albedo and aerosol extinction. An iterative process allows to fit both the smooth continuum, and the water vapor contents (see Figure 10). In spite of a relatively weak absorption due to H_2O in the observed band, the statistical uncertainty of the water vapor retrieval is very low. A large number of measured points within the band (~300) and a relatively high signal-to-noise of SPICAM (from 10 to 150) allow the random uncertainty to measure H_2O as low as a fraction of pr. μm for average spectra. However, systematic uncertain-
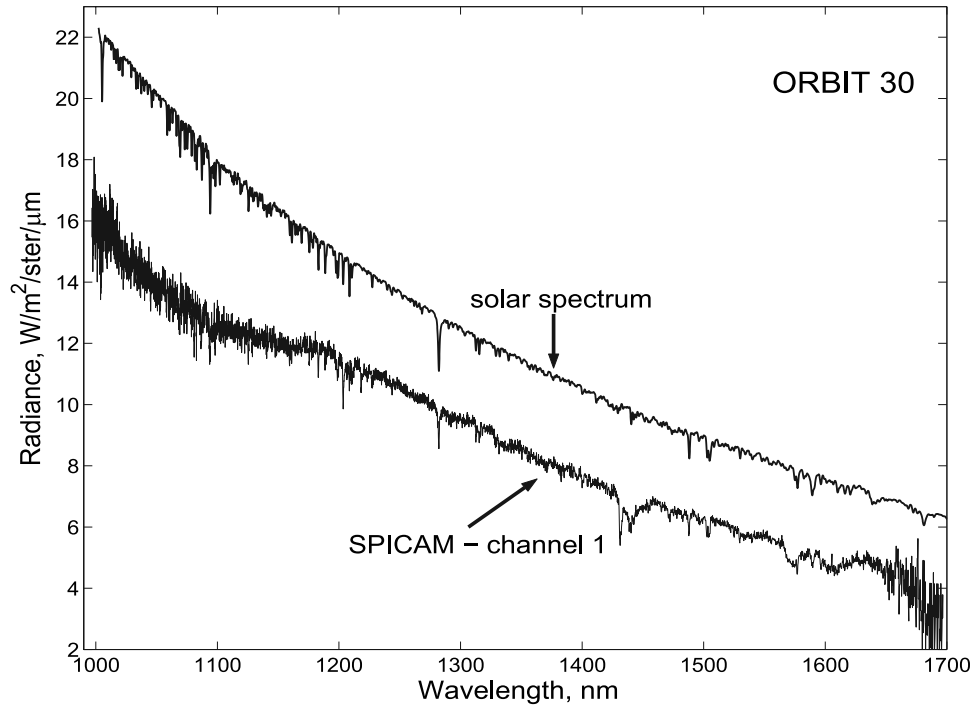
Figure 8. An example of calibrated SPICAM IR spectrum for orbit 30. One individual measured spectrum of Mars is shown compared to the solar spectrum by *Kurucz* [1995]. The solar spectrum is scaled to the Mars data.
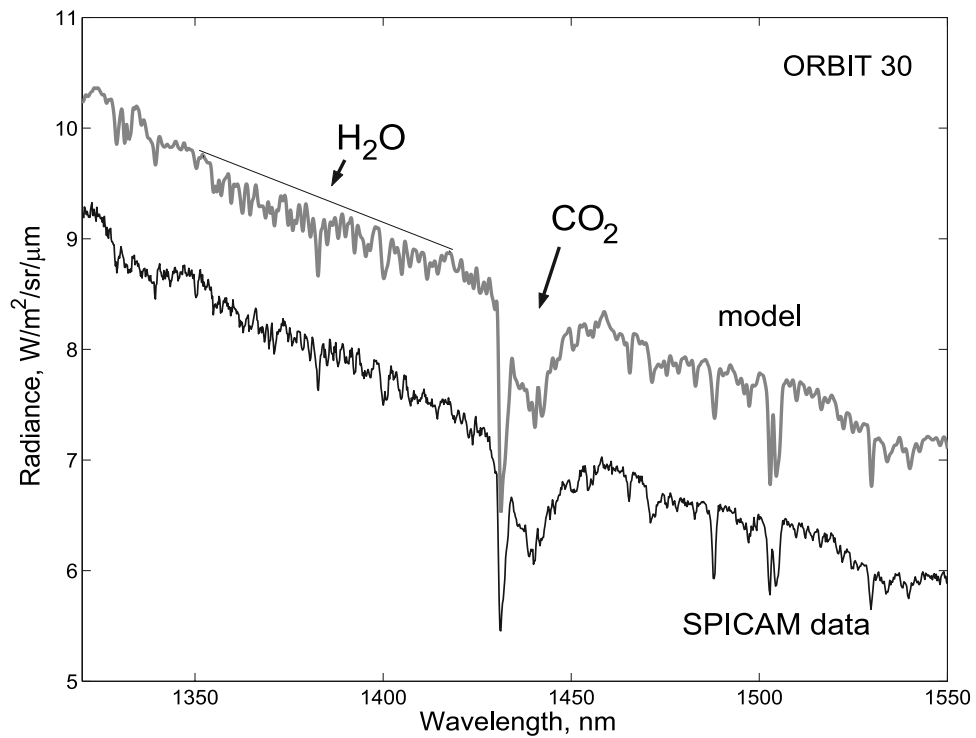
Figure 9. A portion of the spectrum from Figure 7, showing the vicinity of H_2O absorption band at 1.38 μm, and the adjacent CO_2 band at 1.43 μm. Ten subsequent spectra of orbit 30 are averaged together. The synthetic model assumes 8 precipitable microns of atmospheric water. SPICAM spectrum is measured on orbit 30, L_S = 335.7°, latitude 65°S, longitude 58°W, and local time of 0920.
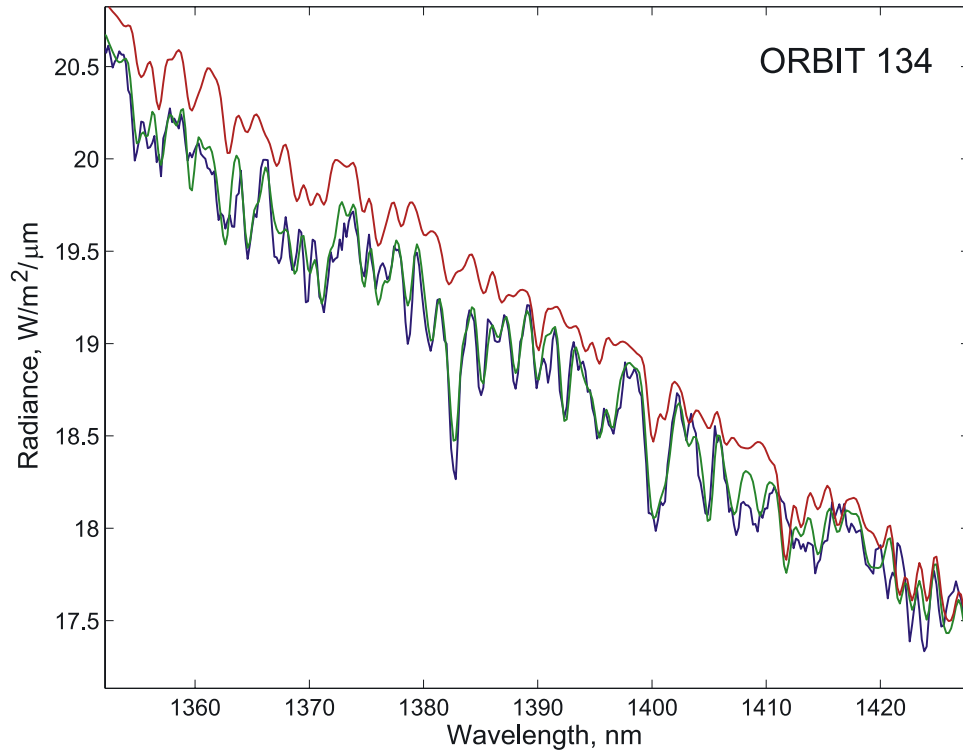
Figure 10. An example of fit to the water vapor band on orbit 134 (L_S = 353.3°, 2.3°N, 139.7°E, local time 1240). The blue curve is the average of six subsequent SPICAM spectra, the red curve is the spectral continuum modified with Sun spectrum, and the green curve is the best fit model, assuming 6.1 pr. microns of water vapor. All the spectral features in this spectral range are due to H_2O absorption or to solar lines.

ties due to spectroscopic and atmospheric model assumptions, radiative transfer in dusty and cloudy atmosphere, instrument calibration, etc., are much higher (5–40%). The discussion on the accuracy, and the details of the retrieval procedure can be found in paper by *Fedorova et al.* [2006a]. Same reference shows a seasonal map of atmospheric water total column contents covering an entire Martian year: January 2004 (Ls = 330°) to November 2005 (Ls = 331°). The maximal measured abundance is 50–55 precipitable microns at the North Pole and 10–15 pr. microns at the South Pole. The northern tropical maximum amounts to 10–15 pr. microns from our data. The seasonal trend of water vapor obtained by SPICAM IR is generally consistent with TES results [*Smith*, 2004]. However, SPICAM shows generally smaller water vapor abundance for all seasons and locations including polar regions, if compared to TES. Possible reasons for the disagreements with TES might be the sensitivity of SPICAM retrievals to the instrument function and to the stray light discussed above, and the effects of scattering by dust, presently ignored. An extended sensitivity analysis is presented by *Fedorova et al.* [2006a].

4.2. Oxygen $O_2(a^1\Delta_g)$ Emission at 1.27 μm

[40] A dayglow 1.27 μm $O_2(a^1\Delta_g)$ emission was predicted just after the discovery of ozone on Mars and it was first observed from the ground by *Noxon et al.* [1976]. The mapping of this emission was reported [*Krasnopolsky and*

Bjoraker, 2000]; *Krasnopolsky* [1997] argues that the O_2 emission provides even better insight to photochemistry than total ozone, because of its high sensitivity to the variations of the water vapor saturation level. At low altitudes this O_2 emission is totally or partially quenched by collisions with CO_2 molecules; therefore this emission is probing mostly altitudes above 20 km.

[41] The band intensity observed by different authors from the ground varies from 1.5 to 26 Mega Rayleigh (MR) and, indeed, SPICAM IR routinely observes the $O_2(a^1\Delta_g)$ band in Nadir and at the limb of Mars, mostly in the polar regions of the planet. Three spectra recorded along one orbit 262 at different latitudes shown in Figure 11 are different: the reflectance of the surface is different, the shape of the spectrum is different, and finally, an emission feature near 1.27 μm is apparent at spectra 2 and 3. This region zoomed in on in Figure 11 (right) reveals a clear signature of $O_2(a^1\Delta_g)$ band of the Martian atmosphere. The resolving power of the instrument at 1.27 μm is about 2200, that allows to measure accurately not only the highest peak of the O_2 single-delta emission, but to retrieve also the structure of the rest of the band. From these measurements we obtained the first seasonal map of the O_2 emission for a Martian year [*Fedorova et al.*, 2006b]. See the same reference for comparison to the available ground-based observations of the O_2 dayglow. Maximal values of the emission are observed during late winter to early spring at
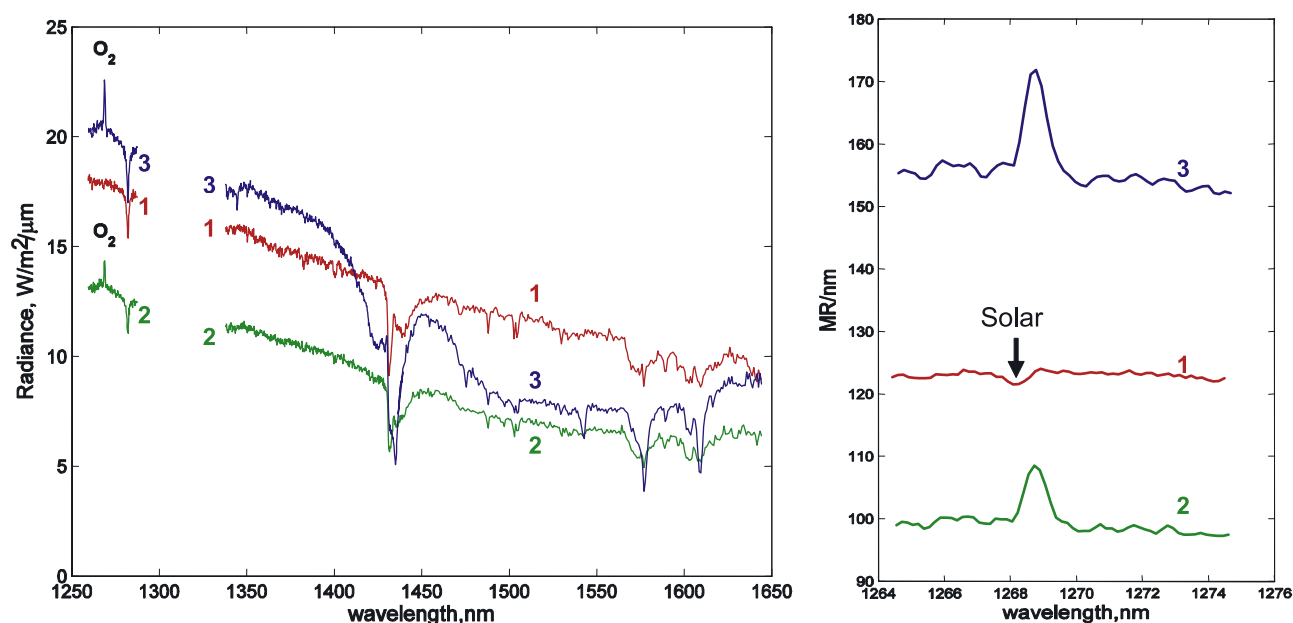
Figure 11. (left) Three spectra measured by SPICAM IR along the orbit 262 ($L_S = 13.3°$) for latitudes of 38°N (curve 1), 58°N (curve 2) and 67°N (curve 3). Spectrum 3 reveals also a broad signature of H_2O ice longward of 1420 nm and CO_2 ice features at 1540, 1578, and 1615 nm (see below). (right) A portion of the spectra, plotted in MegaRayleighs/nm illustrating the high variability of the 1.27 μm $O_2(^1\Delta_g)$ emission in a single orbit.

high latitudes in both hemispheres. Highest dayglow intensity of 26−30 MR is reported in the Southern Hemisphere (70−80°S latitudes) at L_S = 185−195° and in the North polar regions (latitudes 70−80°N) at L_S = 10−20°. In the Southern Hemisphere in summer (L_S = 280−330°) the upper limit for the emission is 1−2 MR. At low latitudes a maximal value of 5−7 MR is observed at L_s = 30−120°.

### 4.3. Early Observations of the South Pole

[42] We present below the results obtained over the south residual cap, on the orbit 30 (18/01/2004) simultaneously with OMEGA [*Bibring et al.*, 2004] and PFS [*Hansen et al.*, 2005] results. The season was late summer in the Southern Hemisphere, L_S = 336°. The seasonal south polar cap has completely disappeared, and the residual polar cap is still illuminated by the Sun. It was simultaneously observed by SPICAM in the UV and the IR spectral ranges. The results of the UV observations are discussed in paper by *Bertaux et al.* [2006]; see there a map of the South pole showing SPICAM IR track on the cap. Here we present the near-IR spectrum of South polar cap. During this measurement, the IR channel was operated in the "full spectrum" mode, and a full IR spectrum is acquired in 24 s. Nine infrared spectra were acquired along the south perennial cap, and the remaining spectra outside of the cap. The distance to the spacecraft during this observation was about 2400 km, the diameter of the instantaneous FOV of the IR spectrometer was 42 km, and the linear extent of the footprint for the entire spectrum was 70−80 km.

[43] With the help of the synthetic model described above, and with the known solar spectrum, we can derive the reflectance of the apparent south cap surface free from gaseous atmospheric absorptions (Figure 12). We could not

claim this is the "true" surface albedo, because some contribution can be due to the atmospheric aerosol, but we estimate that the aerosol contribution does not change the shape of the spectrum significantly.

[44] We compare the obtained spectrum of the surface albedo to laboratory measurements of CO_2 and H_2O pure ices [*Grundy and Schmitt*, 1998; *Quirico and Schmitt*, 1997]. Our albedo spectrum has several distinct features: a broad absorption longward from 1450 nm that that we identify as water ice by comparison with the laboratory spectrum of pure H_2O ice, and a number of conspicuous absorptions, some of them coinciding with gaseous CO_2 absorption bands but having distinctly different shape, attributed to CO_2 ice. The same features are visible in the spectrum recorded in the North polar region (curve 3 in Figure 11). A weak emission near 1270 nm is not the atmospheric $O_2(a^1\Delta_g)$ emission, but an uncompensated solar line, apparent in emission because of imperfect solar spectrum model.

[45] All CO_2 ice absorption lines found in the laboratory spectrum are found in our SPICAM spectrum. The CO_2 ice signatures at 2.28 μm have been observed from the ground already in 1972 [*Larson and Fink*, 1972], see also *Glenar et al.* [2005]. Some information about the distribution of CO_2 and H_2O ice was obtained from Mariner 7 IRS measurements earlier in Martian season (L_S = 200°) [*Calvin and Martin*, 1994]. Our spectra are acquired in the different spectral range, and they also show without ambiguity the presence of both CO_2 and H_2O ices in the South polar cap, simultaneously with OMEGA [*Bibring et al.*, 2004], and PFS [*Hansen et al.*, 2005]. For all our IR spectra we have computed the absorption depth in two wavelength bands: one for the CO_2 band at 1403.6−1435.7 nm, the other for
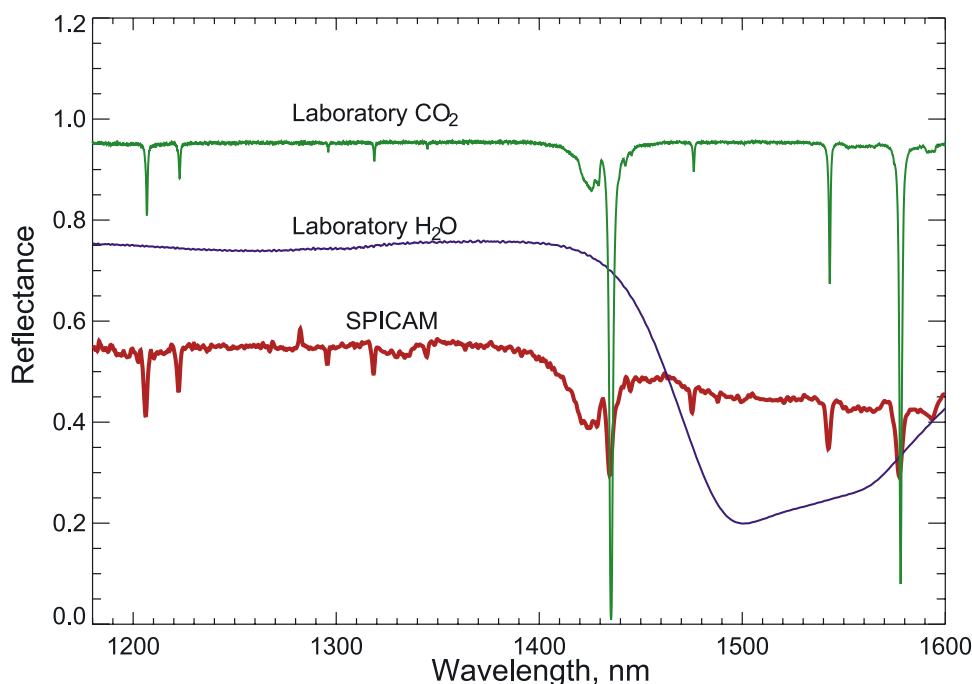
Figure 12. SPICAM IR spectrum recorded at orbit 30 (L_S = 335.7°) near the South Pole of Mars (latitude 85°S). Nine IR spectra recorded over the polar cap have been averaged together. The red curve is the measured spectrum, compared with laboratory transmission spectra showing signatures of both pure CO_2 (green curve) and H_2O ices (blue curve) [*Grundy and Schmitt*, 1998; *Quirico and Schmitt*, 1997]. All CO_2 solid ice features from the laboratory spectrum are found in SPICAM data. The water ice signature is seen as a broad absorption from 1.44 to 1.7 μm. It is not identical to the laboratory curve, possibly an effect of ice temperature, surface texture or grain size. The laboratory spectra are measured for a given thickness of ice, which is likely to be smaller than the light path within polar CO_2 ice (smaller line depth).

the H_2O band at 1481.1−1538.5 nm. Outside the cap, these absorptions are negligible, and on the cap they are somewhat varying with position, but they coexist everywhere.

[46] Our resulting spectrum is a combination of what is seen in the 1° FOV (42 km), but it is also possible that the two ice signatures coexist at a small spatial scale. For instance, we see that the depth of the H_2O signature is smaller in our spectrum than in the laboratory spectrum. This may be due to the simple fact that only a small fractional ground area contains H_2O ice in our 1° FOV. On the contrary, the depth of the CO_2 ice at 1.42 μm is only 4% of that in the laboratory spectrum, while it is 20% in our South Pole spectrum. This might be interpreted in the future in terms of temperature and age of the ice, as well as texture (grain size, or the mean photon path length between scattering points). The high resolution and high S/N ratio of SPICAM IR is an important asset for such a diagnosis. Of particular interest will be the detailed study of the spectral region of 1.45−1.68 μm, where we observe slightly different shape w.r.t. the H_2O ice laboratory absorption spectrum, possibly an indication of clathrate combination of CO_2 and H_2O ices, or temperature effects [*Grundy and Schmitt*, 1998].

[47] The detected of H_2O ice may be present either as a thin layer of condensed atmospheric water vapor coming from the north above the CO_2 ice, or it may represent the bulk of the South polar cap, and being visible at the bottom of "swiss cheese" holes detected on MOC images [*Malin et*

al., 2001]. With the SPICAM spectra, it is difficult to discriminate between the two hypotheses for the origin of the H_2O IR signature within the CO_2 covered polar cap, though they might be both valid.

4.4. Sun Occultation

[48] The useful feature of the SPICAM experiment is the special observation mode: star and sun occultation. The sensitivity of the IR SPICAM is insufficient for stellar occultations which are performed in the UV. Sun occultations are observed simultaneously in the UV and the IR. Solar occultations in the IR should deliver information about vertical distribution of aerosols and water vapor. These measurements are also potentially sensitive to CO_2 and H_2O ice features in atmosphere.

[49] We achieved solar occultations after a number of attempts to direct the "solar" axis of SPICAM to the Sun. In the infrared the task is even more complicated than in the UV, because of smaller FOV and the lack of an imaging detector. Unfortunately the recorded solar spectra have not permitted vertical retrievals of water vapor profiles in most of the cases. One explanation for this might be uncalibrated absorptions observed in these spectra: unlike on the ground, the spectra recorded via the solar entry of SPICAM IR in-flight reveal some quasiperiodic fringes with amplitude comparable or larger than the depth of H_2O absorption features. We associate these fringes with interference, which may arise within the solar entry optical path. These fringes
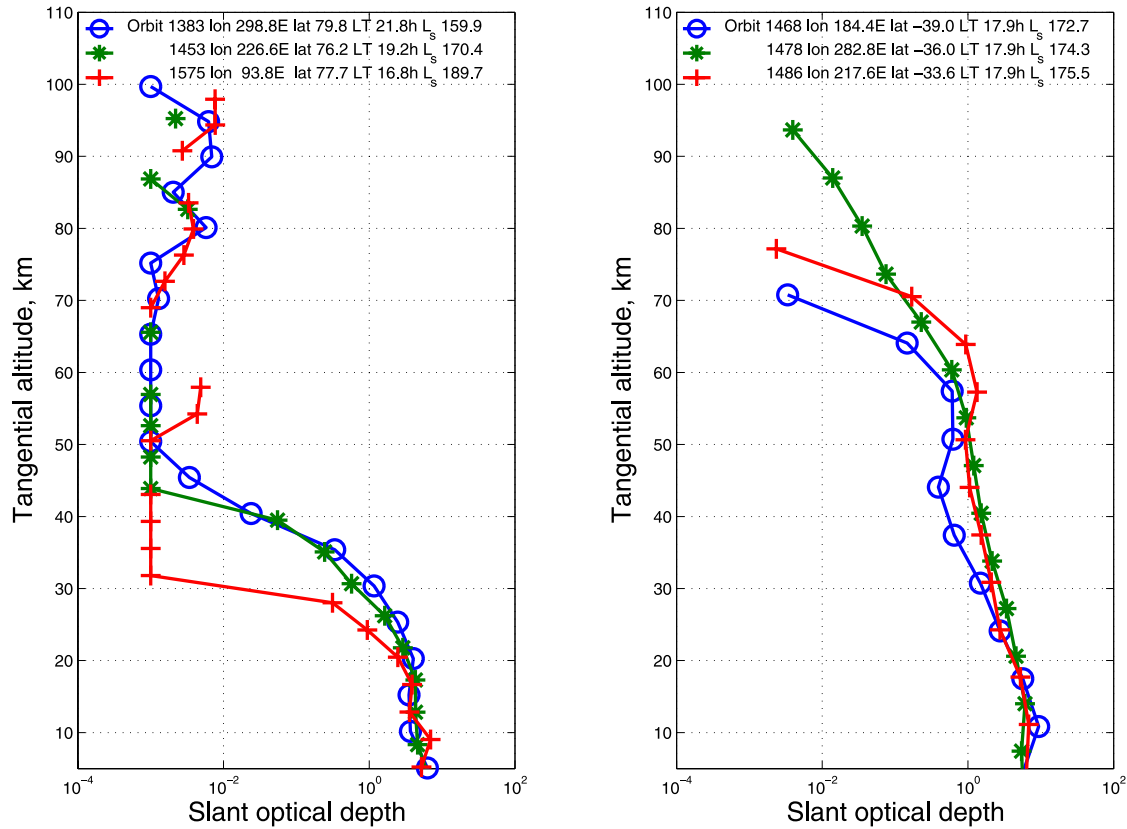
Figure 13. Slant optical depth at the wavelength of 1274 nm measured by SPICAM IR channel in solar occultation profiling. (left) Lower north polar profiles contrast to large extension of dust observed at (right) midlatitudes in the Southern Hemisphere.

disappear in relative spectra divided by an out-of-atmosphere reference spectrum, but some distortion remains, likely due to temperature drift. With more dependable data on the tangent altitude we have understood the origin of the problem. The first solar occultation data were obtained at $L_S = 140°$ to $L_S = 227°$. The vertical extension of dust during this season has been never measured in any Mars mission. In Figure 13 we present some examples of slant optical depth of the Mars atmosphere. At the wavelength of 1274 nm no gaseous absorption is expected, and the extinction is due to aerosol absorption. Although the period of a high dust load in the atmosphere normally begins around $L_S = 180°$ [*Smith*, 2004], we observe rather dense aerosol extending up to 50–70 km (Figure 13, right). Extinction profiles are lower in the North polar area (Figure 13, left), but we detect no water, because during the polar night the atmospheric temperature is low and the water freezes out. Typically slant optical depth reaches unity at the altitudes 35–50 km, and the low signal-to-noise ratio at lower altitudes prevents from measuring water vapor concentrated beneath the atmospheric aerosols and dust. Later in the mission, occultations were performed at midlatitudes, where the vertical extent of the dust is lower, and the absorption due to water vapor is detectable. These data will be analyzed elsewhere.

[50] Sun occultations give direct information about opacity on the line of sight. The quality of the IR photometry is good, and the vertical profiles of aerosol extinction are retrieved for all solar occultation sequences along with spectral behavior of the aerosol in the range of 1–1.65 μm. Vertical extinctions were obtained with a latitude coverage ranging from high latitudes in the Southern Hemisphere to north polar profiles.

5. Conclusions

[51] The described water vapor detector, our first experience with an AOTF spectrometer in a planetary mission is the most simple point spectrometer with a one-pixel detector. This instrument has fully demonstrated the capability of mapping the H_2O contents in the atmosphere [*Fedorova et al.*, 2006a]. The use of the tunable filter implies sequential registration of a spectrum, and a relatively large measurement time, during which the spectrum could change because of the orbital motion. This drawback, to our mind, is fully compensated by such advantages as flexible sampling within the spectral range, and the modulation capability of the AOTF, minimizing the stray light. The AOTF spectrometer is very rugged and stable device, and it contains no moving parts. Besides H_2O measurements, the exited state of O_2 due to photodissociation of ozone is routinely measured [*Fedorova et al.*, 2006b]. Additionally we detect the signatures of H_2O and CO_2 ices, characterizing the conditions on the surface and in the atmosphere (Figure 14).

[52] We believe, that the concept of the instrument capable to measure a number of important atmospheric and environmental characteristic from the orbit on Mars
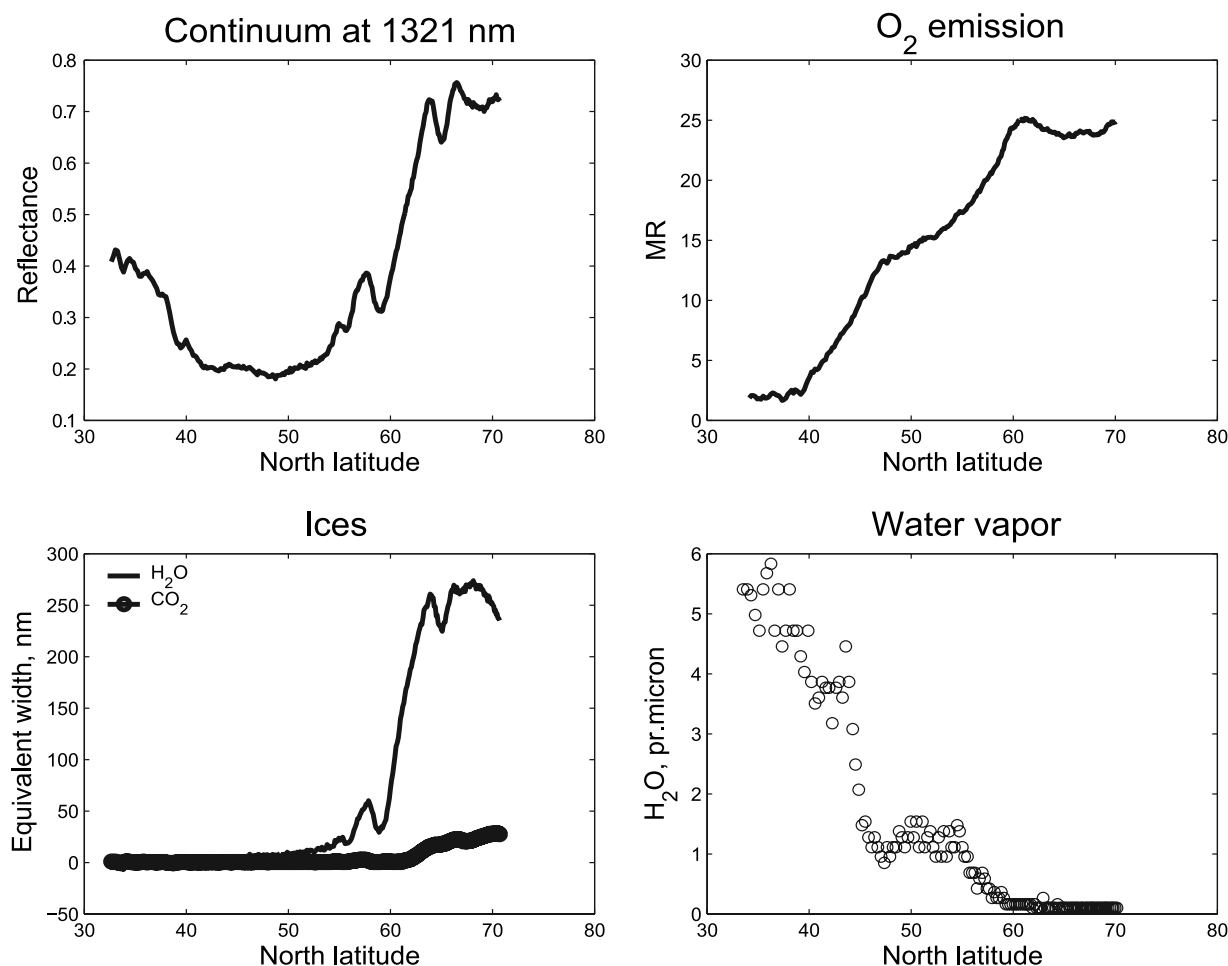
Figure 14. "Products" of SPICAM IR in Nadir observations (orbit 262 L_S = 13.3°, longitude 10°W): spectral continuum at 1321 nm (example wavelength), which is a combination of surface albedo and the aerosol contribution, the intensity of $O_2(a^1\Delta_g)$ emission due to photodissociation of ozone, equivalent the width of carbon dioxide and water ices (on the surface or in aerosol layers), and water vapor total column amount.

or from a lander for less than 1 kg with a potential to upgrade to an imaging spectrometer has a great future. With a mass of only 0.75 kg, this instrument should fly as a low-cost passenger on all future missions to Mars.

References

Bertaux, J. L., et al. (2000), The study of the Martian atmosphere from top to bottom with SPICAM Light on Mars Express, *Planet. Space Sci.*, *48*, 1303–1320.

Bertaux, J. L., et al. (2004), SPICAM Light: An experiment to study the global structure and composition of the Martian atmosphere, *Eur. Space Agency Spec. Publ., ESA-SP 1240*, 95–120.

Bertaux, J. L., et al. (2006), SPICAM on board Mars Express: Instrument, operations, observing modes, and overview of typical results, *J. Geophys. Res.*, doi:10.1029/2006JE002690, in press.

Bibring, J. P., et al. (2004), Perennial water ice identified in the south polar cap of Mars, *Nature*, *428*, 627–630.

Calvin, W. M., and T. Z. Martin (1994), Spatial variability in the seasonal south polar cap of Mars, *J. Geophys. Res.*, *99*(E10), 21,143–21,152.

Chang, I. C. (1981), Acousto-optic tunable filter, *Opt. Eng.*, *20*, 824–828.

Chang, I. C. (1997), Tuneable acousto-optic filters: An overview, *Opt. Eng.*, *16*(5), 455–460.

Chanover, N. J., C. M. Anderson, C. P. McKay, P. Rannou, D. A. Glenar, J. J. Hillman, and W. E. Blass (2003), Probing Titan's lower atmosphere with acousto-optic tuning, *Icarus*, *163*, 150–163.

Colburn, D. S., J. B. Pollack, and R. M. Haberle (1989), Diurnal variations in optical depth at Mars, *Icarus*, *79*, 159–189.

Epikhin, V. M., F. L. Vizen, and V. I. Pustovoit (1984), Acousto-optic filter, Patent of Russia 1247816, 22 pp., Byull. Otkrytiya, Izobreteniya, Moscow, 22 Oct.

Evans, K. F. (1998), The spherical harmonics discrete ordinate method for three-dimensional atmospheric radiative transfer, *J. Atmos. Sci.*, *55*, 429–446.

Farmer, C. B., and D. D. LaPorte (1972), The detection and mapping of water vapor in the Martian atmosphere, *Icarus*, *16*, 34–46.

Fedorova, A., et al. (2006a), Mars water vapor abundance from SPICAM IR spectrometer: Seasonal and geographic distributions, *J. Geophys. Res.*, doi:10.1029/2006JE002695, in press.

Fedorova, A., et al. (2006b), Observation of O_2 1. 27 μm dayglow by SPICAM IR: Seasonal distribution for first Martian year of Mars Express, *J. Geophys. Res.*, doi:10.1029/2006JE002694, in press.

Fiorenza, C., and V. Formisano (2005), A solar spectrum for PFS data analysis, *Planet. Space Sci.*, *53*, 1009–1016.

Forget, F., et al. (1999), Improved general circulation models of the Martian atmosphere from the surface to above 80 km, *J. Geophys. Res.*, *104*(E10), 24,155–24,176.

Formisano, V., et al. (2005), The Planetary Fourier Spectrometer (PFS) onboard the European Mars Express Mission, *Planet. Space Sci.*, *53*, 963–974.

Gass, P. A., and J. R. Sambles (1991), Accurate design of a noncollinear acousto-optic tunable filter, *Optic Lett.*, *16*(6), 429–431.

Georgiev, G., D. A. Glenar, and J. J. Hillman (2002), Spectral characterization of acousto-optic filters used in imaging spectroscopy, *Appl. Opt.*, *41*, 209–217.

Glenar, D. A., J. J. Hillman, B. Saiff, and J. Bergstralh (1994), Acouto-optic imaging spectropolarimery for remote sensing, *Appl. Opt.*, *33*, 7412–7424.

Glenar, D. A., G. Hansen, G. Bjoraker, M. Smith, J. Pearl, and D. Blaney (2005), Bright-region radiative properties with the Mars south polar cap (Ls = 231) from near-infrared spectroscopic imaging, *Icarus*, *174*, 600–603.

Goutzoulis, A. P., and D. R. Pape (Eds.) (1994), *Design and Fabrication of Acousto-Optic Devices*, CRC Press, Boca Raton, Fla.

Grundy, W., and B. Schmitt (1998), The temperature-dependent near-infrared absorption spectrum of hexagonal H_2O ice, *J. Geophys. Res.*, *103*, 25,809–25,822.

Gupta, N. (1997), Acousto-optic tuneable filters, *Opt. Photonics News*, *11*, 23–27.

Hansen, G., et al. (2005), PFS-MEX observation of ices in the residual South Polar cap of Mars, *Planet. Space Sci.*, *53*, 1089–1095.

Korablev, O., J.-L. Bertaux, A. Grigoriev, E. Dimarellis, Y. Kalinnikov, A. Rodin, C. Muller, and D. Fonteyn (2002a), An AOTF-based spectrometer for the studies of Mars atmosphere for Mars Express mission, *Adv. Space Res.*, *29*(2), 143–150.

Korablev, O. I., J. L. Bertaux, E. Dimarellis, A. Grigoriev, Y. Kalinnikov, A. Stepanov, and S. Guibert (2002b), AOTF-based spectrometer for Mars atmosphere sounding, in *Infrared Spaceborne Remote Sensing X*, edited by M. Strojnik and B. F. Andresen, *Proc. SPIE Int. Soc. Opt. Eng.*, *4818*, 261–271.

Krasnopolsky, V. A. (1997), Photochemical mapping of Mars, *J. Geophys. Res.*, *102*(E6), 13,313–13,320.

Krasnopolsky, V. A., and G. L. Bjoraker (2000), Mapping of Mars $O_2(^1\Delta)$ dayglow, *J. Geophys. Res.*, *105*(E8), 20,179–20,188.

Kurucz, R. (1995), The solar spectrum: Atlases and line identifications, in *Workshop on Laboratory and Astronomical High resolution Spectra*, *Astron. Soc. of the Pac. Conf. Ser.*, vol. 81, edited by A. J. Saival, R. Blomme, and N. Grevesse, pp. 17–31, Astron. Soc. of the Pac., San Francisco, Calif.

Larson, H. P., and U. Fink (1972), Identification of carbon dioxide frost on the Martian polar caps, *Astrophys. J. Lett.*, *171*, L91–L95.

Malin, M. C., M. A. Caplinger, and S. D. Davis (2001), Observational evidence for an active surface reservoir of solid carbon dioxide on Mars, *Science*, *294*, 2146–2148.

Noxon, J. F., W. A. Traub, N. P. Carleton, and P. Connes (1976), Detection of O_2 airglow emission from Mars and the Martian ozone abundance, *Astrophys. J.*, *207*, 1025–1035.

Ockert-Bell, M. E., J. F. Bell III, J. B. Pollack, C. P. Mckay, and F. Forget (1997), Absorption and scattering properties of the Martian dust in the solar wavelengths, *J. Geophys. Res.*, *102*(E4), 9039–9050.

Ohmachi, Y., N. Uchida, and N. Niizeki (1972), Acoustic wave propagation in TeO_2 single crystal, *J. Acoust. Soc. Am.*, *51*, 164–168.

Olberg, M., et al. (2003), The Odin satellite. II. Radiometer data processing and calibration, *Astron. Astrophys.*, *402*, L35–L38.

Quirico, E., and B. Schmitt (1997), Near-infrared spectroscopy of simple hydrocarbons and carbon oxides diluted in solid N_2 and as pure ices: Implications for Triton and Pluto, *Icarus*, *127*, 354–378.

Rothman, L. S., et al. (2003), The HITRAN molecular spectroscopic database: Edition of 2000 including through 2001, *J. Quant. Spectrosc. Radiat. Transfer*, *82*, 5–44.

Smith, M. D. (2004), Interannual variability in TES atmospheric observations of Mars during 1999–2003, *Icarus*, *167*, 148–165.

Smith, P. H., and M. Lemmon (1999), Opacity of the Martian atmosphere measured by the imager for Mars Pathfinder, *J. Geophys. Res.*, *104*(E4), 8975–8985.

Thuillier, G., M. Hersé, D. Labs, T. Foujols, W. Peetermans, D. Gillotay, P. C. Simon, and H. Mandel (2003), The solar spectral irradiance from 200 to 2400 nm as measured by the SOLSPEC spectrometer from the Atlas and Eureca missions, *Sol. Phys.*, *214*(1), 1–22.

Voloshinov, V. B., and N. Gupta (1999), Acousto-optic imaging in the mid-infrared region of the spectrum, *Proc. SPIE Int. Soc. Opt. Eng.*, *3900*, 62–73.

Zhang, H., X. L. Wang, J. I. Soos, and J. A. Crisp (1995), Design of a miniature solid state NIR spectrometer, *Proc. SPIE Int. Soc. Opt. Eng.*, *2475*, 376–383.

———————————

J.-L. Bertaux, E. Dimarellis, J. P. Dubois, F. Montmessin, S. Perrier, and A. Reberac, Service d'Aéronomie du Centre National de la Recherche Scientifique, BP 3, F-91371 Verrières-le-Buisson, France.

A. Fedorova, A. Grigoriev, V. Jegoulev, A. Kiselev, and O. Korablev, Space Research Institute, 84/32 Profsoyuznaya, 117810 Moscow, Russia. (korab@iki.rssi.ru)

D. Fonteyn and E. Van Ransbeeck, Belgian Institute for Space Aeronomy, 3 av. Circulaire, B-1180 Brussels, Belgium.

B. Gondet, Institut d'Astrophysique Spatiale, F-91405 Orsay, France.

Y. Kalinnikov, NPP AFAR, 124460 Zelenograd, Russia.

A. Rodin, Moscow Institute of Physics and Technology, Institutsky dr. 9, 141700 Dolgoprudnyi, Russia.

A. Stepanov, Faculty of Physics, Moscow State University, GSP-2, Leninskiye Gory, 119992 Moscow, Russia.